Nuclear Physics A400 (1983) 435c-450c.

RESEARCH HIGHLIGHTS WITH THE SPIN SPECTROMETER

D.G. Sarantites, M. Jääskeläinen[a]), F.A. Dilmanian, H. Puchta[b]), and R. Woodward

Department of Chemistry, Washington University, St. Louis, MO 63130

and

J.R. Beene, D.C. Hensley, M.L. Halbert, J. Hattula[a]), J.H. Barker[c]), and R. Novotny[d])

Oak Ridge National Laboratory, Oak Ridge, TN 37830

and

L. Adler, R.K. Choudhury, M.N. Namboodiri, R.P. Schmitt, and J.B. Natowitz

Cyclotron Institute and Department of Chemistry, Texas A & M University, College Station, TX 77840

Abstract: The excitation energy and angular momentum dependence of the entry states in fusion reactions measured with the spin spectrometer is discussed. A new decay mode involving the onset of localized stretched dipole radiation at half the accompanying stretched E2 collective radiation is found in $^{157-161}$Yb. The appearance of this mode correlates smoothly with neutron number and spin. Possible interpretations are presented in terms of the evolution of the nuclear shapes from prolate to aligned-quasiparticle oblate to collective oblate and then to triaxial. Evidence for nuclear deformation that increases with spin at very high excitation is presented based on α-particle angular distributions measured relative to the spin direction, using a new method for deriving the spin alignment.

1. Introduction

The Spin Spectrometer - for those in the audience that have not heard about it or seen it - is a 4π NaI(Tl) γ-ray detector system segmented in 72 equal solid angle elements covering 96.8% of 4π[1-3]). The instrument records on an event-by-event basis, the pulse height and time of every element that fires, thus providing the total pulse height (related to the γ-ray excitation energy), the γ-ray multiplicity, M_γ, (related to the transferred angular momentum I, at least for reactions leading to deformed rotational nuclei), and the angular correlations of the γ-rays in each event that can give the direction of Spin I. Neutron pulses are effectively rejected by time-of-flight[3]).

I will discuss some of the results from the first generation of experiments in which the spectrometer is triggered by either a single γ-ray observed in one Ge(Li) counter for exit-channel selection or by an α-particle detected in one of several ΔExE telescopes, The first experiments were aimed at exploring the capabilities of the spectrometer by determining the population of the entry states in fusion reactions and then studying their decay. In the first part of my talk I will describe results giving the population distributions of the entry states and their implication about the entrance channel ℓ-distributions leading to fusion. In the second part I will discuss some new and rather unexpected evidence on the systematic variation of the decay mode of the entry states with spin and neutron number. I will then present a possible interpretation of these results in terms of evolution of nuclear shapes with spin and neutron number. Finally, in the last part of my talk, I will summarize some exciting results on the first evidence for nuclear deformation at excitations of 81 MeV above the yrast line,

based on α-angular distributions with respect to the spin direction using a novel technique for deriving the spin alignment.

2. Population of the entry states

I should remind you that since ∿1965 heavy ion reactions and formation of high-spin states were always discussed in terms of populations in (E*,I) space, based only on statistical model calculations[4-6]). The first experimental measurements of the two-parameter population in the closely related (E*,M_γ) space did not come until very recently[7]).

An example of this is shown in fig. 1 from the 136-MeV ^{20}Ne bombardment of

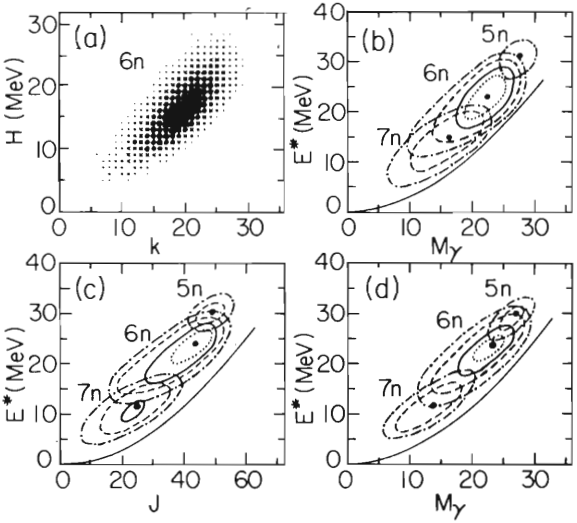

Fig. 1 Entry-state population distributions for the xn products from 136-MeV ^{20}Ne + ^{150}Nd.

(a) Experimental $Q_{6n}(H,k)$ density map for ^{160}Yb.

(b) Contour maps of the experimental entry-state populations in (E^*,M_γ) space for the strongest xn channels.

(c) Contour maps of the calculated populations in (E^*,I) space.

(d) Contour maps in (E^*,M_γ) space from the same calculations as in (c). The cross-section contours decrease by factors of 1.4, 2.0, 4.0 and 8.0 relative to the maximum value of the 6n channel and are given by the dotted, full, dashed and dash-dotted curves, respectively. The heavy dots depict the maxima in the respective channels. The yrast line of ^{160}Yb used in the calculations is shown by the curve below the contours.

^{146}Nd. Fig. 1a shows a density plot of the entry state distribution $Q_{6n}(H,k)$ for the (^{20}Ne,6n) exit channel in terms of H, the total pulse height in 1-MeV steps, and the coincidence fold k. The unfolded distributions in terms of E* and M_γ are shown as contour plots in fig. 1b and are obtained by the procedure described in ref. 3). The displacement of the distributions toward higher E* and M_γ with decreasing number of emitted neutrons is clearly seen, but there is considerable overlap between adjacent channels. These main features are well reproduced by statistical model calculations with the Monte Carlo code JULIAN-PACE[8]) modified to include a more realistic treatment of γ-ray emission. The initial ℓ distributions were taken to be of the form

$$(2\ell+1)\ (1 + \exp\frac{\ell-\ell_{fus}}{d})^{-1}$$

The level density parameter was taken as a=A/9.5. The yrast lines were taken

from the rotating liquid drop model[9]) (RLDM) above spin 22, but below that value the moment of inertia was decreased linearly with I to approximate the behavior of real rotational nuclei. The El γ-ray emission strength included the giant dipole resonance[10-12]) with its shape and position derived from systematics[12-14]) and its strength determined by the energy-weighted sum rule[14]). Statistical E2 and M1 transitions were included with strengths of B(E2)=1.0 W.u. and B(M1)=0.005 W.u., together with collective E2 transitions with B(E2)=100 W.u. for E_γ<2.0 MeV. The Monte Carlo γ cascades proceeded to the vicinity of the yrast line and are then assumed to reach the ground state on an yrast state with I<2 by stretched E2 transitions[8]). The calculated and experimental M_γ distributions are compared in figs. 2a and 2b with good overall agreement. The best agreement with the total (sum of

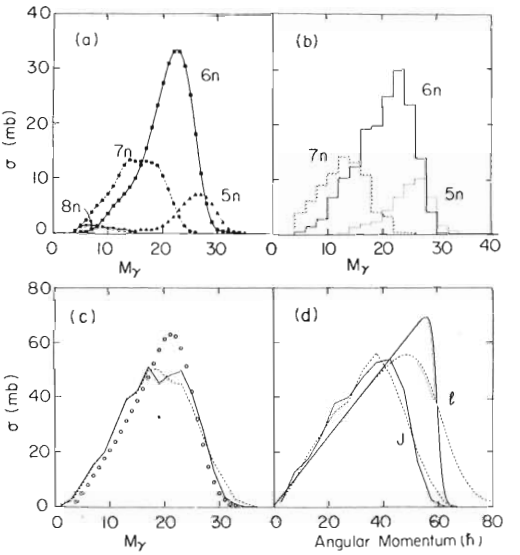

Fig. 2 Projections of the entry-state populations.
(a) Experimental cross sections for the xn channels as a function of M_γ.
(b) Calculated cross sections (ℓ_{fus}=59.5 and d=1) for the xn channels as a function of M_γ.
(c) Experimental cross sections (points) and calculated distributions (lines) for the sum of xn and αx channels as a functions of M_γ.
(d) Entrance channel and the resulting I distributions summed over all the xn and αxn channels. The dashed and solid lines in (c) and (d) are for d=1 and d=5 respectively.

xn and αxn channels) M_γ distributions were obtained for ℓ_{fus}=59.5 and d≤2. The solid and dashed lines in fig. 2c and 2d correspond to d=1 and 5, respectively. The ℓ-distributions with d≤2 exhibit a fairly sharp cut-off in the upper edge.

A simpler way of comparing the measured and calculated populations of figs. 1b and 1d is to plot the entry lines <E*> vs. <M_γ>. The entry lines from three different reactions are shown in fig. 3.

The calculated entry lines were obtained with the same set of parameters that gave the best fit to the 136 MeV data. Good agreement is seen for the positions and the slopes for the main part of the entry lines in fig. 3a. For the reactions at higher bombardment energy the calculated entry lines lie at somewhat higher energies, but this is not significant, since no effort was made to fit the data in detail. At the higher multiplicities the experimental entry lines exhibit a significant decrease in slope observed at M_γ=21,22,23,25 and 27 for the ^{157,158,159,160,161}Yb, respectively. This change in slope depends only on the nuclide formed and not on the reaction used to produce it. This effect cannot be reproduced by any reasonable variation of the parameters used in the

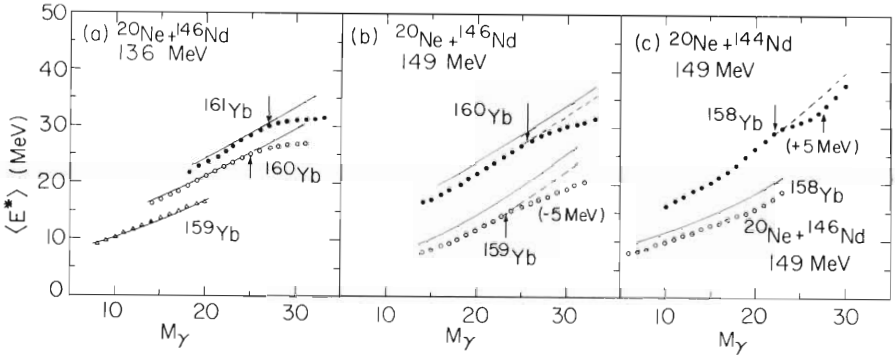

Fig. 3 Experimental (points) and calculated (solid lines) entry lines $\langle E^* \rangle$ vs. $\langle M_\gamma \rangle$, for $^{159-161}$Yb from (a) 136-MeV and (b) 149-MeV reactions of ^{20}Nd, and (c) for ^{158}Yb from 149 MeV reactions of ^{20}Ne on ^{144}Nd (shifted up by 5 MeV) and ^{146}Nd. The dashed lines are empirical curves showing extrapolations of smooth curves through the data in order to locate the positions of the onset of change in slope. They are essentially parellel to the calculated entry lines.

statistical model calculations, unless a drastic change in the decay mode or a rapid increase in the effective moment of inertia in the product nuclei is invoked. These two possibilities should affect in a different way the γ-ray spectra associated with the decay of the entry states.

3. Decay of the entry states

3.1 EXPERIMENTAL OBSERVATIONS

The decay of the entry states was investigated by constructing γ-ray spectra using all the NaI detectors in the spectrometer for each coincidence fold k. Information about the multipole character of the γ-rays under the assumption that only stretched dipole and stretched quadrupole radiation contribute was derived from pulse height spectra taken for each k with five groups of detectors at 24.4°, 45.6°, 65.7°, 77.5°, and 87.3° (and their supplements) with respect to the beam. These spectra were in coincidence with the $2^+ \rightarrow 0^+$ or the $17/2^+ \rightarrow 13/2^+$ yrast transitions in the product nuclei observed with the Ge(Li) counter. The contribution of the underlying Compton background was subtracted. The NaI pulse-height spectra were unfolded to produce the γ-ray energy spectra, by an iterative unfolding procedure that takes into account the response of the detectors. The detector response functions were constructed from sources with γ-ray energies between 0.136 and 4.439 MeV and included the effects of coincidence summing and crystal-to-crystal scattering appropriate to each pulse-height spectrum[7]). The γ-ray multiplicities appropriate for each spectrum were derived from the response functions for the spectrometer $P(E^* M_\gamma \rightarrow Hk)$ and the deduced entry state populations, $R_x(E^*, M_\gamma)$, as discussed in detail in ref. 3).

Some γ-ray spectra, normalized to their respective multiplicities are shown in fig. 4.

The spectra from ^{161}Yb shown in fig. 4a exhibit the expected behavior[6]) for rotational rare earth nuclei with N≥92. A bump is observed with an upper edge which moves in a regular fashion to higher energies as M_γ increases up to ≈27. The angular distribution of these γ-rays is consistent with stretched quadrupole radiation. At higher M_γ a spike of stretched dipole character develops at ∼700 keV. Despite the presence of these localized dipole transitions, the upper edge of the quadrupole bump continues to move to higher E_γ in the highest M_γ

spectra. The onset of the localized dipole component with an energy (∿0.7 MeV) of about half of that of the quadrupole component explains the decrease in slope of the entry line (fig. 3a) which appears at the same M_γ. The observation of these dipole transitions also excludes the possibility of a regular rotational behavior with a rapidly increasing moment of inertia with increasing spin.

The change in the decay mode as M_γ increases becomes progressively more pronounced in the successively lighter Yb isotopes. In ^{160}Yb for M_γ up to 25 the spectra show an evolving bump (fig. 4b), which for all E_γ is entirely consistent with stretched E2 transitions, as it is seen from the anisotropies given in fig. 5a for M_γ=16-19. For M_γ >25 the γ-spectra show the localization of the additional transitions at ∿650 keV and the continued but somewhat slower evolution to higher E_γ of the edge of the quadrupole bump. The transitions localized at 650 keV are clearly dipole in character as seen from the anisotropies (fig. 5b, $M_\gamma \geq 26$). The anisotropy information together with difference spectra constructed from successive multiplicities allow us to deduce a dipole to quadrupole ratio of (0.9±0.2):1.0. Again, the presence of these dipole transitions accounts for the decrease in slope of the entry line in fig. 3a and 3b. The constant slope of the entry line for M_γ >27 indicates that the ratio of dipole to quadrupole transitions is nearly constant up to the highest M_γ values reached.

The spins associated with each M_γ value were derived with the aid of the statistical-model calculations. The rotational picture used in the calculations reproduces the slopes of the entry line below the onset of the localized dipole radiation. In this region the average spin for each M_γ was obtained from the calculated entry lines as a function of M_γ and of I using the expression

$$\langle I \rangle = [\Sigma_I \; I \cdot S(I,M_\gamma)]/\Sigma_I \; S(I,M_\gamma)$$

where $S(I,M_\gamma)$ is the calculated distribution connecting I to M_γ. For higher M_γ the additional stretched ΔI=1 transitions were accounted for by changing the $M_\gamma \rightarrow I$ mapping above the point of change in slope by a factor of ∿0.75 corresponding to equal numbers of dipole and quadrupole transitions. This procedure gives for the onset of the change in the decay mode the values of I≃50 ($M_\gamma \simeq 27$) and I≃45 ($M_\gamma \simeq 25$) in ^{161}Yb and ^{160}Yb, respectively. The presence of the dipole transitions also explains the apparent slower evolution

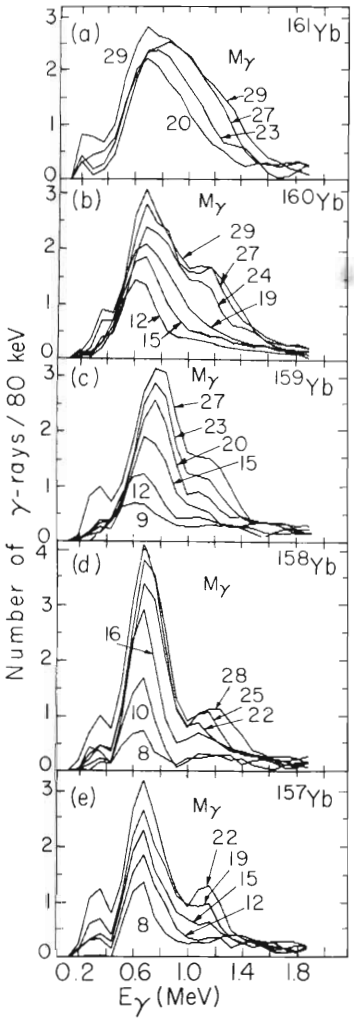

Fig. 4 Continuum γ-ray spectra of $^{161-157}$Yb for selected M_γ as shown obtained in the reactions: (a) ^{146}Ne(^{20}Ne,8n) at 136 MeV, (b) ^{146}Ne(^{20}Ne,6n) at 136 and 149 MeV, (c) ^{146}Nd(^{20}Ne,7n) at 136 and 149 MeV, (d) ^{144}Nd(^{20}Ne,6n) and ^{146}Nd(^{20}Ne,8n) at 149 MeV, and (e) ^{144}Nd(^{20}Ne,7n) at 149 MeV.

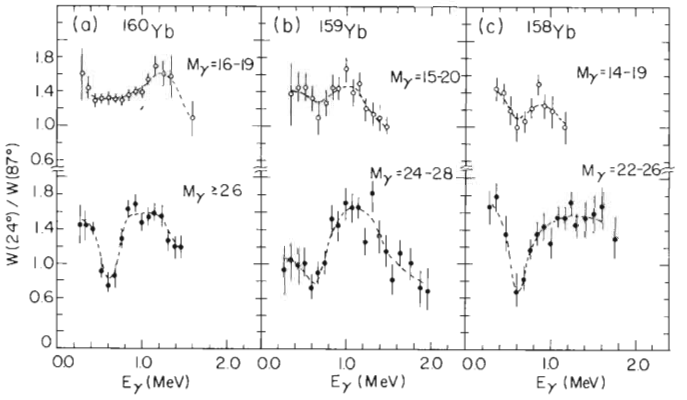

Fig. 5 Anisotropies of the γ-rays of the continuum in (a) ^{160}Yb, (b) ^{159}Yb, and (c) ^{158}Yb for two regions of M_γ. The M_γ values given correspond to the half maximum limits of the k gates selected.

of the quadrupole edge with M_γ because now $\Delta I/\Delta M_\gamma \approx 1.5$. With the correct $M_\gamma \rightarrow I$ mapping a smooth dependence of the effective moment of inertia $\mathcal{J}_{eff}$ on I is obtained as shown in fig. 6a. Here we have derived $\mathcal{J}_{eff}$ from the mid point of the upper edge of the quadrupole bump, assuming rotational behavior. The smooth evolution of $\mathcal{J}_{eff}$ with I in the range of I=45-54 is completely consistent with collective rotational behavior. If the presence of dipoles is ignored in the $M_\gamma \rightarrow I$ mapping, erroneously large $\mathcal{J}_{eff}$ values result at the highest spins.

As the neutron number is decreased going to lighter Yb isotopes, the appearance of the dipole component shifts at lower spins as seen from the results in figs. 3 and 4. For ^{159}Yb and ^{158}Yb this change in decay mode occurs at $M_\gamma \approx 23$ (I≈42) and $M_\gamma \approx 22$ (I≈40), respectively. In addition to this, another interesting phenomenon is observed in ^{158}Yb. For $M_\gamma < 22$ the entry line from ^{144}Nd(^{20}Ne,6n)^{158}Yb at 149 MeV shows the expected slope, which at $M_\gamma = 22$ decreases and then for $M_\gamma = 28$ it increases, taking a value close to that for $M_\gamma < 22$. Two prominent features are seen in the γ spectra from the ^{144}Nd(^{20}Ne,6n)^{158}Yb and ^{140}Nd(^{20}Ne,8n)^{158}Yb reactions at 149 MeV (fig. 4d). The first involves a bump at $E_\gamma \sim 500$-900 keV, which evolves smoothly up to $M_\gamma \approx 20$. The second is the appearance above $M_\gamma \approx 22$ of another higher energy bump with an upper edge reaching $E_\gamma \approx 1.4$ MeV at $M_\gamma \approx 28$. The behavior of these two bumps with increasing M_γ, when correlated

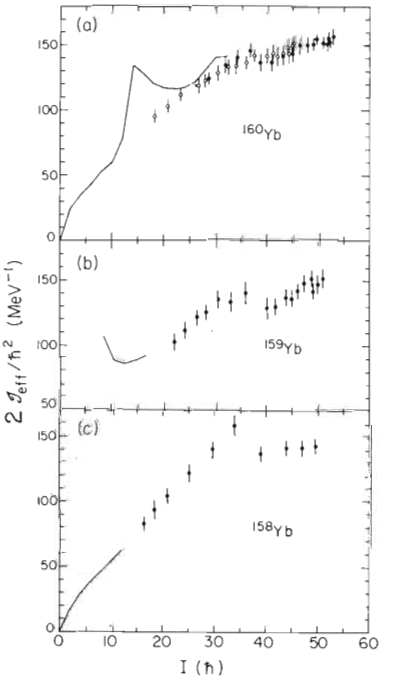

Fig. 6 Effective moment of inertia $\mathcal{J}_{eff}$ as a function of spin I for ^{160}Yb (a), ^{159}Yb (b), and ^{158}Yb (c). The lines give $\mathcal{J}_{eff}$ from known yrast levels.

with the shape of the entry line (fig. 3c) and the angular distributions (fig. 4c) provides the following consistent picture for the de-excitation of ^{158}Yb. The yrast decay for ^{158}Yb is known[15]) up to the $I^{\pi}=12^{+}$ state and consists of a cascade of stretched E2 transitions (E_{γ} from 358 to 683 keV). The evolution of the upper edge of the lower energy bump is consistent with the continuation of a predominant quadrupole cascade up to $M_{\gamma}\approx 18$ ($I\approx 32$). However, the angular distributions for $M_{\gamma}=14$-19 in fig. 5c are less anisotropic than would be predicted for stretched E2 transitions suggesting the presence of some dipoles. This is also supported by the small difference in the slopes of the calculated and observed entry lines in fig. 3c for the ^{20}Ne+^{146}Nd reaction. In addition, below $M_{\gamma}\approx 20$ difference spectra from successive M_{γ} bins indicate that the additional γ-rays contribute not only on the upper edge but also to the peak of the bump. For $M_{\gamma}\approx 15$ to 20 the additional transitions span the range of 0.5 to 1.0 MeV. All these features suggest a tendency toward an aligned-quasiparticle structure, characteristic of nuclei with small oblate deformations[16]), for $I\approx 25$-40 in ^{158}Yb. This description is consistent with recent results on the yrast states for ^{158}Yb up to $I=32$.[17])

An entirely different behavior in the de-excitation of ^{158}Yb is observed above $M_{\gamma}\approx 22$, where the decrease in the slope of the entry line is seen (figs. 4d and 3c). The additional γ-rays between $M_{\gamma}\approx 22$-28 are localized in two different energy regions at the lower half of the intense bump and in a new bump at $E_{\gamma}\sim 1.3$ MeV well above the upper edge of the intense bump. The angular distributions of the γ-rays between $M_{\gamma}=22$-26 in fig. 5c clearly show a dipole character for the lower energy component and a quadrupole character for the higher energy one. From the difference spectra, the angular distributions and the shape of the entry line, we conclude that the dipoles are localized to a narrow region of 650±100 keV and that 3 to 4 of the additional 6 transitions between $M_{\gamma}=22$ and 28 are dipole. The E2 transitions are also localized to a region $\sim$200 keV wide the center of which moves from $\sim$1.1 MeV to $\sim$1.3 MeV as the M_{γ} increases from 22 to 27. These observations clearly indicate that the decay mode of the entry states for ^{158}Yb between $M_{\gamma}\approx 22$ to 27 ($I\approx 40$ to 49) is the same as the decay mode of ^{159}Yb, ^{160}Yb and ^{161}Yb above $I\approx 42$, 45 and 50, respectively.

Still another change in the decay mode of ^{158}Yb is observed at the highest multiplicities, $M_{\gamma}>27$. The growth of the dipole component of 650 keV decreases sharply at $M_{\gamma}\approx 27$ ($I\approx 49$) while the high energy quadrupole component continues to evolve up to the highest M_{γ} reached. This explains the observed increase in slope in the entry line above $M_{\gamma}\approx 28$ back to that characteristic of quadrupole radiation.

After the appearance of the localized dipole component, the evolution of the quadrupole bump to higher E_{γ} is very similar for all the Yb isotopes studied, and constitutes a new component not connected to the continuation of the rotational behavior observed at the lower spins. This is seen clearly from the $\mathcal{J}_{\text{eff}}$ values shown in figs. 6b and 6c as a discontinuity. For lower spins and below the onset of the dipole component ^{157,158}Yb decay differently as discussed earlier, whereas ^{160,161}Yb and perhaps ^{159}Yb decay as expected for good rotors.

3.2 INTERPRETATION

We have presented evidence for the systematic variation of a new decay mode in the $^{157-161}$Yb isotopes with neutron number and nuclear spin. This new mode sets in at $I\approx 38$, 40, 42, 45, and 50 in the N=87, 88, 89, 90, and 91 isotopes of Yb, respectively, and is manifested by the appearance of a localized dipole component at half the energy of a new collective quadrupole component. Unlike the evolution to higher E_{γ} of the quadrupole component, the evolution of the dipole component has not been observed. It should be $\lesssim$100 keV, which is well within the gating resolution of the instrument, and thus cannot be excluded.

Detailed calculations for the structure of the $^{158-164}$Yb isotopes, based on a cranked modified-oscillator shell model, have been performed by Andersson *et al.*[18]). These results for ^{158,160}Yb and interpolated curves for ^{157,159,161}Yb are shown in fig. 7 by the solid lines. We can use these predictions for a

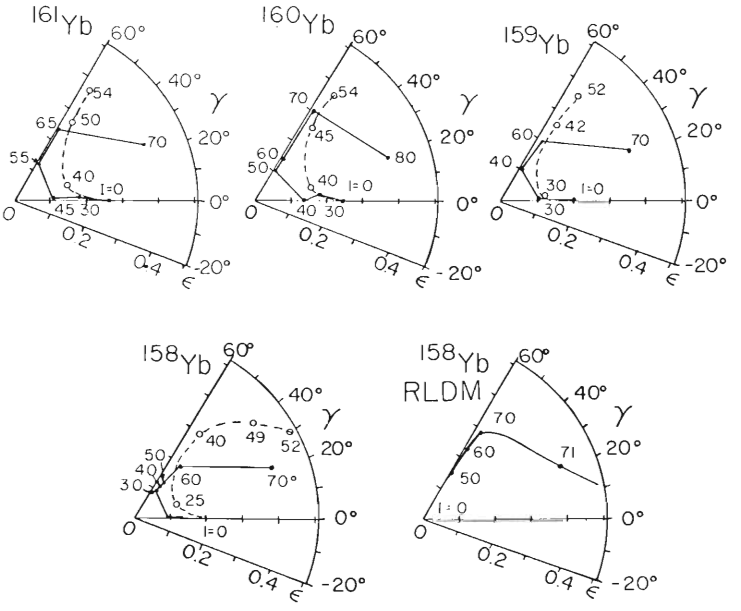

Fig. 7 Trajectories in the (ε,γ) plane of the equilibrium shapes for the Yb isotopes from ref. 18) (solid lines). Trajectories for odd A were interpolated. The dashed line gives a pictorial representation of the shape changes in a possible interpretation of the data. The dots and open circles give the spins defining the trajectories.

possible interpretation of the changes in the decay mode that we observed. Near the ground states all the Yb isotopes should be prolate due to the effects of pairing. At higher spins a systematic decrease in deformation along the prolate axis ($\gamma \approx 0°$) is predicted. As the spin is further increased, a sudden change to oblate shape is predicted for the lighter Yb isotopes, which moves smoothly to higher spins as N is increased. At the higher spins, evolution back toward the prolate shapes is predicted via intermediate triaxial configurations. Thus ^{160}Yb is predicted to change to oblate between I=40 and 50 and remain oblate up to I=70, whereas ^{158}Yb is predicted to change to oblate at lower spins and then become triaxial above $I \approx 50$.

The observed spectra from ^{157,158}Yb at I≈20-32 suggest a behavior such as that seen in the N=88 ^{154}Dy[19]) and ^{158}Yb[17]) with a rotational behavior at the lower spins followed by the onset of an irregular behavior characteristic of a particle-aligned oblate structure ($\varepsilon \approx 0.1$) seen in ^{152}Dy[20]). This is in accord with the calculations shown in fig. 7. These calculations lead us to expect that the strongly localized stretched dipole radiation is associated with the oblate shapes, since all the nuclei studied are predicted to be oblate in the spin region where we observe the dipoles. The strong localization of the dipole transitions near half the energy of the coincident collective quadrupole radiation indicates that they may be transitions in collective bands. For oblate nuclei, whatever their deformation, the yrast states are most likely due to aligned quasiparticle states with their spin along the symmetry axis. Upon these K≈I states collective bands could be built. Such states are not expected to have appreciable collectivity for $|\varepsilon| < 0.25$, but they could be important for larger

deformations[21]). The excited states in these bands will not be yrast, but could lie close to the yrast line. In fact, intraband M1 transitions in high K-bands are favored in the rotational model which predicts $B(M1) \propto K^2$ and $B(E2) \propto 1/K$.

The arguments given above suggest an interpretation of the behavior of the $^{157-161}$Yb nuclei in terms of these calculations. The behavior of ^{157,158}Yb at lower spins was already discussed. The new decay mode associated with the localized dipole radiation can be tentatively identified with oblate deformations having $|\varepsilon| \geq 0.3$ which set in at I≈38, 40, 42, 34 and 50 in ^{157,158,159,160,161}Yb, respectively. For A≥159 it appears that a transition to the $\gamma \approx 60°$ axis (oblate) occurs with deformation large enough to allow collective motion. The spins at which this transition occurs in each Yb isotope as a function of $|\varepsilon|$ agree quantitatively with the theory. All the Yb isotopes are expected to become triaxial at sufficiently high spin. For ^{158}Yb this change is predicted to occur within the range of spins observed in our measurements. Interestingly, only for ^{158}Yb was the disappearance of the dipole radiation observed at I≈49. This may be evidence for the evolution toward triaxiality, thus providing further correspondence between experiment and theory. A plausible path for the evolution of spin is shown by the dashed curves in fig. 7 using the ε values as we discussed. The correspondence between experiment and theory as a function of spin and neutron number is remarkable with the following exceptions. Firstly, our speculative interpretation requires a significant increase in $|\varepsilon|$ along the oblate axis for ^{157,158}Yb, but a constant deformation is predicted for ^{158}Yb in the same spin range. Secondly, we must invoke larger deformations for the oblate shapes in all the isotopes compared to those predicted.

The speculative association of the localized dipole radiation with collective bands built on high-K states is not the only mechanism for the production of such dipoles. Another mechanism is the wobbling motion of triaxial nuclei[18]), but those calculations lead to smaller M1/E2 branching ratios and M1 energies higher than half the associated quadrupole transition energies. Recent systematic RPA calculations of the wobbling motion for ^{158}Yb have been reported[22]). These calculations require a relatively large deformation ε=-0.3 in order to reproduce the energy of the dipole radiation in the K range from 40 to 50. However, larger dipole energies are obtained[22]) for ε=-0.12 than is preferred from earlier calculations[18,23]).

It is quite clear that further experiments and more detailed microscopic calculations are needed in order to provide the correct interpretation of our results.

4. Nuclear deformation from α-particle angular distributions with respect to the spin direction

4.1 THE SPIN ALIGNMENT METHOD

Knowlege of the shape of the nucleus at high excitation and its dependence on spin is a subject of considerable current interest[24,25]). We expect that nuclei at many tens of MeV of excitation will be almost uninfluenced by pairing and shell effects[26]) so that their behavior with spin might be closely approximated by the prediction of the RLDM[9]). The nuclear shapes of highly excited nuclei can be investigated by measurements of evaporated α particles since they are emitted in the first steps of the de-excitation process[25,27]).

The reaction of 176.6 MeV ^{20}Ne on ^{150}Nd was used and α particles were measured in nine Si surface-barrier ΔE,E telescopes (two at 80° and one at 90° to the beam, ∿89° and 97° in CM). The ΔE detectors had a thickness of 75 μm and an acceptance cone of ∿6° half angle. A Si detector at 8° detected evaporation residues in coincidence with the telescopes.

We have used the Spin Spectrometer to determine both the magnitude and the direction of the spin on an event-by-event basis. The method used to determine the spin direction for each event is based on the fact that the γ cascades from rotational nuclei emit a preponderance of stretched E2 transitions which exhibit a "doughnut"-like angular distribution about the spin direction given by

$W(\theta_\gamma)=(5/4)(1-\cos^4\theta_\gamma)$ (see fig. 8a). Assuming that the spin lies in the plane perpendicular to the beam direction (fig. 8b), we project the γ pattern for each

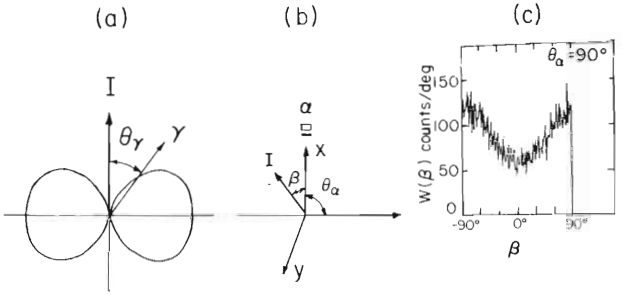

Fig. 8 (a) Angular pattern of stretched E2 radiation about the spin direction.
(b) Schematic representation of the geometry of the measurement.
(c) Angular distribution of the α particles about the spin direction. Alternately this is frequency of spin orientations relative to the direction of the α particles.

event on that plane and then use elaborate centroid searching routines to find the angle specifying the symmetry axis of the projected "peanut"-like pattern. The uncertainty in the deduced spin direction of the evaporation residues (ER) comes from the finite multiplicity M_γ, the fraction of stretched E2 transitions in the cascade, the finite solid angle of the NaI detectors, the γ-ray scattering, and the coincidence summing. The finite aperture of the α detectors contributes to the uncertainty in the angle between the spin of the evaporation residue and the direction of the α particles. Furthermore, the loss of spin alignment due to non-stretched particle emission contributes to the uncertainty in the angle β (fig. 8b). All these effects were incorporated in a Monte Carlo simulation of the spin response function $P(\beta,M_\gamma)$. Two examples of this are shown in fig. 9a for M_γ=13 (10 stretched E2 + 3 stretched dipoles) and for M_γ=29 (22 stretched E2 and 7 stretched dipoles).

4.2 ANGULAR DISTRIBUTIONS OF α-PARTICLES ABOUT THE SPIN DIRECTION

An angular distribution of α particles about the spin direction recorded for one telescope at θ_α=90° is shown in fig. 8c. It corresponds to all α energies and to 20 or more NaI detectors firing in the spectrometer ($k\geq 20$). Spectra of α particles were measured for five equal bins of 18° in β for each of the following five bins in the γ-ray coincidence fold k: 11-14, 15-18, 19-22, 23-26, and 27-33. The k values were converted to M_γ and then to the spin of the evaporation residues using the procedure described above (see also refs. 3 and 7). These k bins correspond to the spin ranges of ∿14-29, 23-37, 32-44, 40-49, and 46-55 for the evaporation residues. The average spins $\langle I_i \rangle$ of the α-emitting nucleus that lead to the k bins chosen were calculated with the JULIAN-PACE code[8]) and were found to be ∿34, 43, 51, 59 and 64, respectively. Multiplicity distributions in coincidence with α-particles only and with events gated by coincidences between α-particles and evaporation residues were found to be identical, indicating absence of significant contributions from deep inelastic re-

actions or fission. The energy spectra of the α partciles were transformed to the center-of-mass for α + ^{160}Er. The center-of-mass spectra from the 80° and 150° telescopes were similar below 27 MeV indicating absence of non-equilibrium contributions for $E_\alpha \leq 27$ MeV in the 80° and 90° telescopes. The angular distributions from the two telescopes at 89° and the one at 97° in CM were combined. Fig. 10 shows examples of α-spectra for β=9° and 81° relative to the spin direction. The enhanced yield at 81° for E_α=14 MeV by a factor of 1.6 relative to that at the Coulomb barrier (21 MeV for spherical nucleus) is apparent. Experimental angular distributions relative to the spin direction $W(\beta, E_\alpha, M_\gamma)$ were fitted to

$$A_o[1 + A_2P_2(\cos\beta) + A_4P_4(\cos\beta)].$$

The angular distributions for 14 and 21 MeV alphas corresponding to $\langle I_i \rangle$=34 and 59 (k bins of 11-14 and 23-26) are shown in fig. 9b together with their fits. The enhancement of α-emission in the direction perpendicular to the spin direction is apparent. It is seen to increase substantially for the sub-barrier alphas. The energy and spin dependence of this effect is best illustrated in fig. 11 where the A_2 coefficients are plotted vs. $E_{\alpha,CM}$ for the five spin gates.

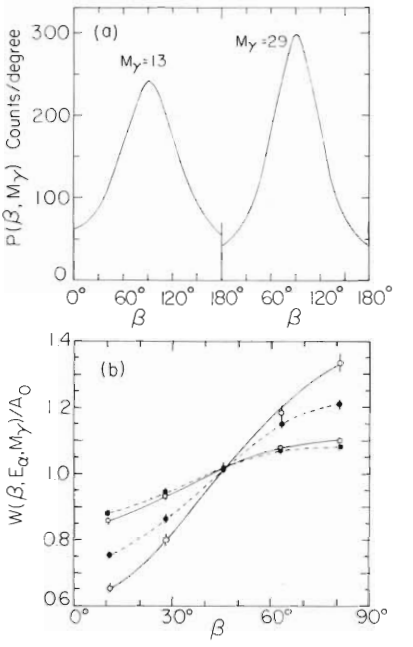

Fig. 9 (a) Examples of simulated spin response functions for finding the spin direction on an event-by-event basis.

(b) Experimental angular distributions of α particles with respect to the spin direction. The open and closed squares correspond to E_α=14 and 21 MeV, respectively, for k=11-14 bin (I∿34). The open and closed circles correspond to E_α=14 and 21 MeV, respectively, for the k=23-26 bin (I∿59). The solid and dashed lines give the least-squares fits of $A_0[1 + A_2P_2 + A_4P_4]$ to the data.

4.3 EVIDENCE FOR DEFORMATION

In order to understand the observed enhancement in α emission at 90° to the spin direction (A_2 more negative) for E_α below and above the barrier, we have carried out detailed calculations of the angular distributions using transmission coefficients from a spherical optical potential.

The α-particle distribution for an initial spin I_i, a final spin I_f, and energy E_α is given by

$$W_{E_\alpha I_i I_f}(\beta) = \sum_\lambda a_{E_\alpha I_i I_f \lambda} B_\lambda(I_i) P_\lambda(\cos\beta) \qquad (1)$$

where

$$a_{E_\alpha I_i I_f \lambda} = \sum_\ell \frac{T_\ell(E_\alpha)}{\sum T_{\ell'}(E_\alpha)} (-1)^{I_i+I_f} (2\ell+1)(2I_i+1)^{1/2}(2\lambda+1)^{1/2} \begin{pmatrix} \ell & \ell & \lambda \\ 0 & 0 & 0 \end{pmatrix} \begin{Bmatrix} \ell & \ell & \lambda \\ I_i & I_i & I_f \end{Bmatrix}$$

Here, $T_\ell(E_\alpha)$ are transmission coefficients, and $B_\lambda(I_i)$ is the statistical tensor describing the ensemble of spin orientations with respect to the quantization

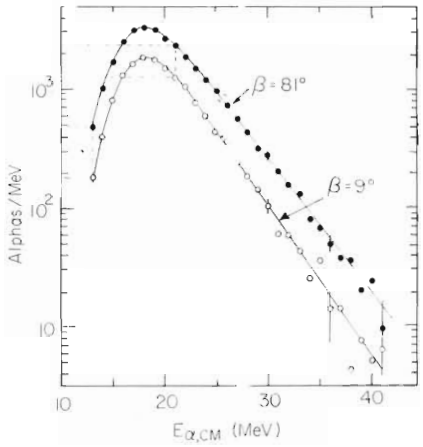

Fig. 10 Examples of α-particle spectra from the k=23-26 bin recorded in a telescope at 80° to the beam and corresponding to the angles of β=9° and 81° with respect to the spin direction. The solid lines guide the eye. The dashed lines depict the difference in the anisotropies near and below the barrier.

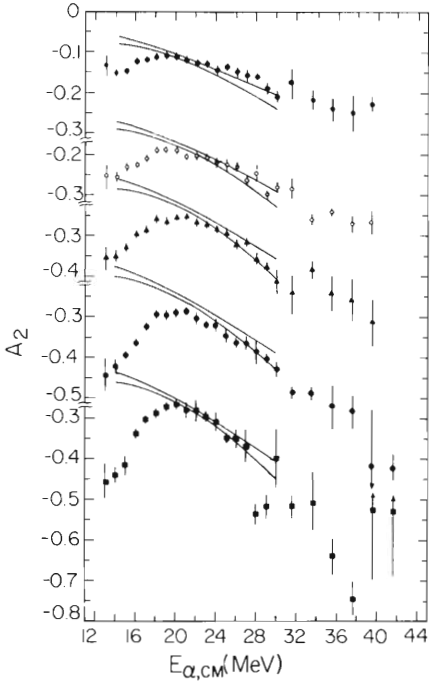

Fig. 11 A_2 coefficients as a function of E_α. The points represent experimental results. Closed and open circles correspond to k bins of 11-14 and 15-18 (I∿34 and 43), respectively. The closed triangles, closed large circles, and closed squares correspond to the k bins of 19-22, 23-26, and 27-32 (I∿51, 59, and 64), respectively. The curves are theoretical A_2 coefficients using $T_\ell(E_\alpha)$ from a spherical optical potential. The double lines in each case reflect the statistical uncertainties due to the Monte Carlo simulation.

axis. We assume that the quantization axis is different for each event and choose it to be the estimated spin direction. In this way $B_\lambda(I_i)$ is determined by the distribution of the true spin directions about this estimate. We obtain $B_\lambda(I_i)$ from $P(\beta,M_\gamma)$, using the vector model to relate β to the magnetic substates of the spin. Angular distributions for comparison with experiment were calculated for various gates on E_α and on M_γ by integrating eq. (1) over distributions of $\Delta I=I_i-I_f$, which are derived from the statistical model simulation using the JULIAN-PACE code with transmission coefficients from a spherical optical potential. The A_2 values calculated in this way are shown in fig. 11 by the solid lines.

The calculated A_2 coefficients agree well with experiment above the Coulomb barrier, but show large discrepancies for low energies (fig. 11). This observation suggests an interpretation in terms of nuclear deformation. For a spherical nucleus A_2 should decrease monotonically (more negative) with increasing E_α for the following reason. The α-angular distribution is determined by the combined effects of the T_ℓ and the level density. As E_α increases, the range on non-zero T_ℓ coefficients extends to higher ℓ values for which the level density favors "stretched" α-transitions (larger ΔI), thus giving small A_2 values (larger 90°/0° ratio). The slope of the A_2 curve is expected to become less steep at the lower energies, because the α-particles below the barrier receive a larger contribution from regions of lower excitation, but still far above the yrast line (table 1), and such cascades are expected to have somewhat larger anisotropies. These trends are observed in the calculated A_2 coefficients (fig. 11) using a spherical nuclear shape. For a deformed nucleus and for E_α below the barrier, however, a geometrical picture for the barrier penetration is more useful. This is because the dominant factor in the anisotropy may well be the penetrability through the potential of the deformed nucleus with a given orientation with respect to the spin direction. If the lowest barrier (i.e., the largest deformation) is at 90° to the spin, then the sub-barrier alphas will be emitted preferentially in that direction. Above the Coulomb barrier the anisotropy is not expected to be as sensitive to deformation, and may approach the value for a spherical nucleus. The results shown in fig. 11 support this interpretation. If we assume that the deviation of the theory from experiment below the barrier is due to deformation, then the increase of this deviation with increasing spin would be an indication for larger deformations as the spin rises.

From these results we cannot at present determine the shape of the α-emitting nucleus. We can, however, eliminate two spheroidal configurations on the basis of the preferred emission 90° to the spin. The excluded shapes are an oblate spheroid rotating perpendicular to its symmetry axis and a prolate one rotating about its symmetry axis. The excitation energies for α emission were estimated from the Monte Carlo simulation, which gave an average excitation energy of 81 MeV above the yrast line for all the α emitting nuclei. The fraction of α particles emitted in first, second and third chance evaporation was 15% (with $\langle E^*\rangle$=135 MeV, 26% (with $\langle E^*\rangle$=124 MeV), and 31% (with $\langle E^*\rangle$=88 MeV), respectively. The remainder of 28% of the α-particles were from fourth or higher chance emission. The excitation energies and spins of the α-emitting nuclei that correspond to evaporation of α particles of various energies were obtained by the Monte Carlo simulation and are summarized in Table 1.

Table 1. Summary of excitation energies and spin of the α-emitting states leading to various E_α values.

E_α(MeV)	$\langle I_i\rangle$	$\langle E^*_i\rangle$(MeV)	$\langle\Delta I\rangle$
14.8	38.1	67.8	4.0
16.6	38.5	80.8	4.0
19.9	41.0	95.4	4.1
>23	43.8	103.2	4.0
All E_α	41.3	93.3	4.0

Because of the high excitation energies involved we can compare our results with the predictions of the RLDM. For a nucleus with Z=70 and A=170 the RLDM predicts a change, beginning at I=81, from an oblate spheroid rotating about its symmetry axis to a triaxial spheroid rotating about its shortest axis, which survives up to I∿84 and then undergoes fission. These two configurations are consistent with our results. According to the RDLM, however, only the oblate shape is expected for the spin values observed, since ℓ_{ER}=68 for this system[28]). A prolate nucleus rotating perpendicular to its symmetry axis is also consistent with the present results. Such a configuration results from pairing and shell effects, but they are likely to be absent at these high excitations[26]). The deformations predicted by the RDLM are ε∿0.1 for the lowest k bin studied (I∿34) and ε∿0.3 for the highest one (I∿64).

This work was supported in part by the U.S. Department of Energy. Oak Ridge National Laboratory is operated by Union Carbide Corporation for the U.S. Department of Energy under contract no. W-7405-eng-26. One of us, H.P., thanks the Deutsche Forschungsgemainshaft for a scholarship.

5. References

a) Present address: Department of Physics, University of Jyväskylä, Jyväskylä, Finland.
b) Present address: Department of Physics, University of Munich, West Germany.
c) Present address: F45, South Carolina Electric and Gas Company, P.O. Box 764, Columbia, SC 29218.
d) Present address: Department of Physics, University of Heidelberg, Heidelberg, West Germany.
1) D.G. Sarantites, R. Lovett, and R. Woodward, Nucl. Instr. and Meth. 171 (1980) 503.
2) D.G. Sarantites, M. Jääskeläinen, J.T. Hood, R. Woodward, J.H. Barker, D.C. Hensley, M.L. Halbert, and Y.D. Chan, Journ. de Phys. 41 (1980) C10.
3) M. Jääskeläinen, D.G. Sarantites, R. Woodward, F.A. Dilmanian, J.T. Hood, R. Jääskeläinen, D.C. Hensley, M.L. Halbert, and J.H. Barker, Nucl. Instr. and Meth. (in press).
4) D.G. Sarantites and B.D. Pate, Nucl. Phys. A93 (1966) 545.
5) J.R. Grover and J. Gilat, Phys. Rev. 157 (1967) 802, 814.
6) R.M. Diamond and F.S. Stephens, Ann. Rev. Nucl. Sci. Part. Sci. 30 (1980) 85, and references therein.
7) D.G. Sarantites, M. Jääskeläinen, R. Woodward, F.A. Dilmanian, D.C. Hensley, J.H. Barker, J.R. Beene, M.L. Halbert, and W.T. Milner, Phys. Lett. B, (in press).
8) Code JULIAN, M. Hillman and Y. Eyal (unpublished); modification PACE by A. Gavron, Phys. Rev. C21 (1980) 230.
9) S. Cohen, F. Plasil, and W.J. Swiatecki, Ann. Phys. 82 (1974) 557.
10) J.H. Barker and D.G. Sarantites, Phys. Rev. C9 (1974) 607.
11) J.O. Newton, et al., Phys. Rev. Lett. 46 (1981) 1383.
12) G.A. Bartholomew, et al., in Advances in Nuclear Physics, eds. M. Baranger and E. Vogt, vol. 7 (1973) p.229.
13) S.S. Hanna, in Giant Multipole Resonances, ed. F. Bertrand (Harwood, New York, 1980), table I.
14) A. Bohr and B.R. Mottelson, in Nuclear Structure, vol. II (W.A. Benjamin, Inc., Reading, MA, 1975) 474 ff.
15) W. Trautmann, D. Proetel, O. Häusser, W. Hering, and F. Reiss, Phys. Rev. Lett. 35 (1975) 1694.
16) A. Bohr and B.R. Mottelson, Phys. Scripta 10A (1974) 13; ibid. 24 (1981) 71.
17) C. Baktash, et al., private communication (1982).
18) G. Andersson, S.E. Larsson, G. Leander, P. Möller, S.G. Nilsson, I. Ragnarsson, S. Åberg, R. Bengtsson, J. Dudek, B. Nerlo-Pomorska, K. Pomorski, and Z. Szymanski, Nucl. Phys. A268 (1976) 205.
19) A. Pakkanen, Y.H. Chung, P.J. Daly, S.R. Faber, H. Helppi, J. Wilson, P. Chowdhury, T.L. Khoo, I. Ahmad, J. Borggreen, Z.W. Grabowski, and D.C. Radford, Phys. Rev. Lett. 48 (1982) 1530.
20) T.L. Khoo, R.K. Smither, B. Haas, O. Häusser, H.R. Andrews, D. Horn, and D. Ward, Phys. Rev. Lett. 41 (1978) 1027.
21) C.G. Andersson and Leander, Lysekil Conf. on nuclear structure, 1979.
22) P. Arve, Y.S. Chen, and G.A. Leander, Nordic Meeting on nuclear physics, Fuglø, 1982 (submitted to Phys. Scripta).
23) R. Bengtsson, S.E. Larsson, G. Leander, P. Möller, S.G. Nilsson, S. Åberg, and Z. Szymanski, Phys. Lett. 57B (1975) 301.
24) M.A. McMahan and J.M. Alexander, Phys. Rev. C21 (1981) 1261.
25) M. Blann and T.T. Komoto, Phys. Scripta 24 (1981) 93.
26) A. Bohr and B. Mottelson, in Nuclear Structure, vol. II (W.A. Benjamin, New York, 1975).
27) J.R. Grover and J. Gilat, Phys. Rev. 157 (1967) 823.
28) M.L. Halbert, R.A. Dayras, R.L. Ferguson, F. Plasil, and D.G. Sarantites, Phys. Rev. C17 (1978) 155.